Editors' Suggestion

Control over Berry Curvature Dipole with Electric Field in WTe_2

Xing-Guo Ye,[1,*] Huiying Liu,[2,*] Peng-Fei Zhu,[1,*] Wen-Zheng Xu,[1,*] Shengyuan A. Yang,[2] Nianze Shang,[1] Kaihui Liu,[1] and Zhi-Min Liao[1,†]

[1]*State Key Laboratory for Mesoscopic Physics and Frontiers Science Center for Nano-optoelectronics, School of Physics, Peking University, Beijing 100871, China*

[2]*Research Laboratory for Quantum Materials, Singapore University of Technology and Design, Singapore, 487372, Singapore*

(Received 30 May 2022; revised 28 September 2022; accepted 18 December 2022; published 4 January 2023)

Berry curvature dipole plays an important role in various nonlinear quantum phenomena. However, the maximum symmetry allowed for nonzero Berry curvature dipole in the transport plane is a single mirror line, which strongly limits its effects in materials. Here, via probing the nonlinear Hall effect, we demonstrate the generation of Berry curvature dipole by applied dc electric field in WTe_2, which is used to break the symmetry constraint. A linear dependence between the dipole moment of Berry curvature and the dc electric field is observed. The polarization direction of the Berry curvature is controlled by the relative orientation of the electric field and crystal axis, which can be further reversed by changing the polarity of the dc field. Our Letter provides a route to generate and control Berry curvature dipole in broad material systems and to facilitate the development of nonlinear quantum devices.

DOI: 10.1103/PhysRevLett.130.016301

Berry curvature is an important geometrical property of Bloch bands, which can lead to a transverse velocity of Bloch electrons moving under an external electric field [1–6]. Hence, it is often regarded as a kind of magnetic field in momentum space, leading to various exotic transport phenomena, such as anomalous Hall effect (AHE) [1], anomalous Nernst effect [7], and extra phase shift in quantum oscillations [8]. The integral of Berry curvature over the Brillouin zone for fully occupied bands gives rise to the Chern number [5], which is one of the central concepts of topological physics.

Recently, Sodemann and Fu [9] proposed that the dipole moment of Berry curvature over the occupied states, known as Berry curvature dipole (BCD), plays an important role in the second-order nonlinear AHE in time-reversal-invariant materials. For transport in the x-y plane which is typical in experiments, the relevant BCD components form an in-plane pseudovector with $D_\alpha = \int_k f_0(\partial_\alpha \Omega_z)$ [9], where D_α is the BCD component along direction α, $\boldsymbol{k}$ is the wave vector, the integral is over the Brillouin zone and with summation over the band index, f_0 is the Fermi distribution (in the absence of external field), Ω_z is out-of-plane Berry curvature, and $\partial_\alpha = \partial/\partial k_\alpha$. It results in a second-harmonic Hall voltage in response to a longitudinal ac probe current, which could find useful applications in high-frequency rectifiers, wireless charging, energy harvesting, and infrared detection, etc. BCD and its associated nonlinear AHE have been predicted in several material systems [9–11] and experimentally detected in systems such as two-dimensional (2D) monolayer or few-layer WTe_2 [12–15], Weyl semimetal $TaIrTe_4$ [16], 2D MoS_2, and WSe_2 [17–20], corrugated bilayer graphene [21], and a few topological materials [22–25]. However, a severe limitation is that BCD obeys a rather stringent symmetry constraint. In the transport plane, the maximum symmetry allowed for D_α is a single mirror line [9]. In several previous Letters [17–21], one needs to perform additional material engineering such as lattice strain or interlayer twisting to generate a sizable BCD. This constraint limits the available material platforms with nonzero BCD, unfavorable for the in-depth exploration of BCD-related physics and practical applications.

Recent works suggested an alternative route to obtain nonzero BCD, that is, utilizing the Berry connection polarizability to achieve a field-induced BCD, where the additional lattice engineering is unnecessary [26,27]. The Berry connection polarizability is also a band geometric quantity, related to the field-induced positional shift of Bloch electrons [28]. It is a second-rank tensor, defined as $G_{ab}(\boldsymbol{k}) = [\partial A_a^{(1)}(\boldsymbol{k})/\partial E_b]$, where $\boldsymbol{A}^{(1)}$ is the field-induced Berry connection, $\mathbf{E}$ is the applied electric field [28], and the superscript "(1)" represents that the physical quantity is the first order term of electric field. Then, the E field induced Berry curvature is given by $\boldsymbol{\Omega}^{(1)} = \nabla_{\mathbf{k}} \times (\overleftrightarrow{\mathbf{G}}\mathbf{E})$ [27], where the double arrow indicates a second-rank tensor. This field-induced Berry curvature will lead to a field-induced BCD $D_\alpha^{(1)}$. Considering transport in the x-y plane and applied dc E field also in the plane, we have $D_\alpha^{(1)} = \int_k f_0(\partial_\alpha \Omega_z^{(1)}) = \varepsilon_{z\gamma\mu} \int_k f_0[\partial_\alpha(\partial_\gamma G_{\mu\nu})]E_\nu$, where $\alpha, \gamma, \mu, \nu = x, y$, and $\varepsilon_{z\gamma\mu}$ is the Levi-Civita symbol. In systems where the original BCD is forbidden by the crystal symmetry, the field-induced BCD by an external E field

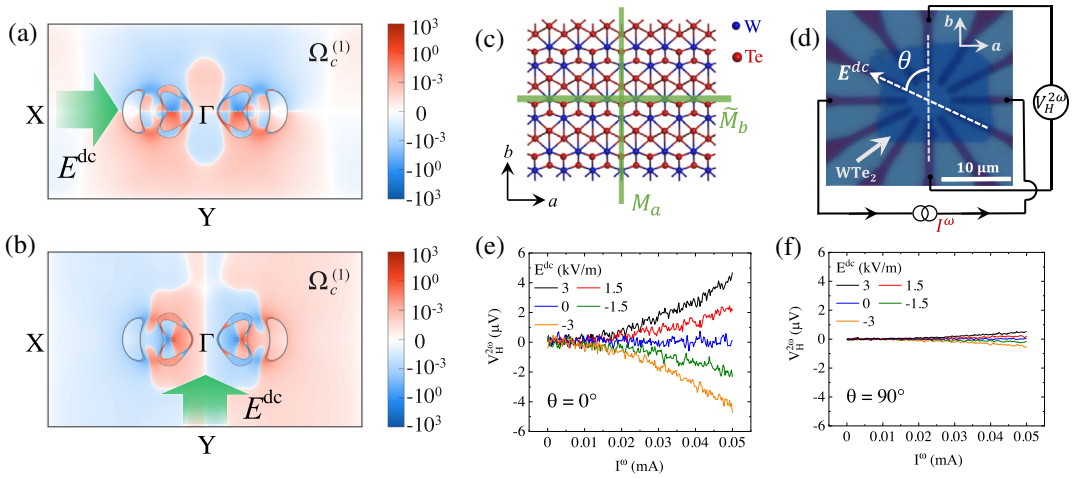

FIG. 1. (a) and (b) The field-induced Berry curvature $\Omega_c^{(1)}(\boldsymbol{k})$ in the $k_z = 0$ plane by a dc electric field $E^{dc} = 3$ kV/m applied along (a) a or (b) b axis, respectively. The unit of $\Omega_c^{(1)}(\boldsymbol{k})$ is Å^2. The green arrows indicate the direction of $\mathbf{E}^{dc}$. The gray lines depict the Fermi surface. (c) The a-b plane of monolayer T_d-WTe_2. (d) The optical image of device S1, where an angle θ is defined. (e) and (f) The second-harmonic Hall voltage $V_H^{2\omega}$ as $\mathbf{E}^{dc}$ (e) along b axis ($\theta = 0°$), and (f) along $-a$ axis ($\theta = 90°$) at 5 K. The $\mathbf{E}^{\omega}$ is applied along $-a$ axis, as schematized in (d).

could generally be nonzero and become the dominant contribution. In such a case, the symmetry is lowered by the applied E field, and the induced BCD should be linear with E and its direction also controllable by the E field. So far, this BCD caused by Berry connection polarizability and its field control have not been experimentally demonstrated yet, and the nonlinear Hall effect derived from this mechanism has not been observed.

In this Letter, we report the manipulation of electric field induced BCD due to the Berry connection polarizability. Utilizing a dc electric field $\mathbf{E}^{\mathrm{dc}}$ to produce BCD in bulk WTe_2 (for which the inherent BCD is symmetry forbidden), the second-harmonic Hall voltage $V_H^{2\omega}$ is measured as a response to an applied ac current I^{ω}. Both orientation and magnitude of the induced BCD are highly tunable by the applied $\mathbf{E}^{dc}$. Our Letter provides a general route to extend BCD to abundant material platforms with high tunability, promising for practical applications.

The WTe_2 devices were fabricated with circular disc electrodes (device S1) or Hall-bar shaped electrodes (device S2). The WTe_2 flakes were exfoliated from bulk crystal and then transferred onto the prefabricated electrodes (Supplemental Material, Note 1 [29]). The WTe_2 thickness of device S1 is 8.4 nm (Supplemental Material, Fig. S1 [29]), corresponding to a 12-layer WTe_2, and we present the results from device S1 in the main text. The crystal orientations of WTe_2 devices were identified by their long, straight edges [12] and further confirmed by both polarized Raman spectroscopy (Supplemental Material, Note 2 [29]) and angle-dependent transport measurements (Supplemental Material, Note 3 [29]). The electron mobility of device S1 is ~ 4974 cm^2/V s at 5 K (Supplemental Material, Note 4 [29]).

In our experiments, we use thick T_d-WTe_2 samples (thickness $\sim$8.4 nm), which have an effective inversion symmetry in the x-y plane (which is the transport plane). This is formed by the combination of the mirror symmetry M_a and the glide mirror symmetry $\tilde{M}_b$, as indicated in Fig. 1(c). The in-plane inversion leads to the absence of inherent in-plane BCD and hence the nonlinear Hall effect in bulk (see Supplemental Material, Note 5 [29] for detailed symmetry analysis). Because $\tilde{M}_b$ involves a half-cell translation along the c axis and hence is broken on the sample surface, a small but nonzero intrinsic BCD may exist on the surface. In fact, such BCD due to surface symmetry breaking has already been reported [13], and is also observed in our samples, although the signal is much weaker in thicker samples (see Supplemental Material, Fig. S9 [29]).

To induce BCD in bulk WTe_2 through Berry connection polarizability, a dc electric field $\mathbf{E}^{\mathrm{dc}}$ is applied in the x-y plane. As shown in Figs. 1(a) and 1(b), the field-induced Berry curvature shows a dipolelike distribution with nonzero BCD (theoretical calculations; see Supplemental Material, Note 6 [29]). The induced BCD can be controlled by the dc E field and should satisfy the following symmetry requirements. Because the presence of a mirror symmetry would force the BCD to be perpendicular to the mirror plane [9], the induced BCD $\mathbf{D}^{(1)}$ must be perpendicular to $\mathbf{E}^{\mathrm{dc}}$ when $\mathbf{E}^{\mathrm{dc}}$ is along the a or b axis. Control experiments were carried out in device S1 to confirm the above expectations. The measurement configuration is shown in Fig. 1(d) (see Supplemental Material, Fig. S2 [29], for circuit schematic). The probe ac current with ac field $\mathbf{E}^{\omega}$ and frequency ω was applied approximately along the $-a$ axis, satisfying $E^{\omega} \ll E^{\mathrm{dc}}$, and the second-harmonic Hall

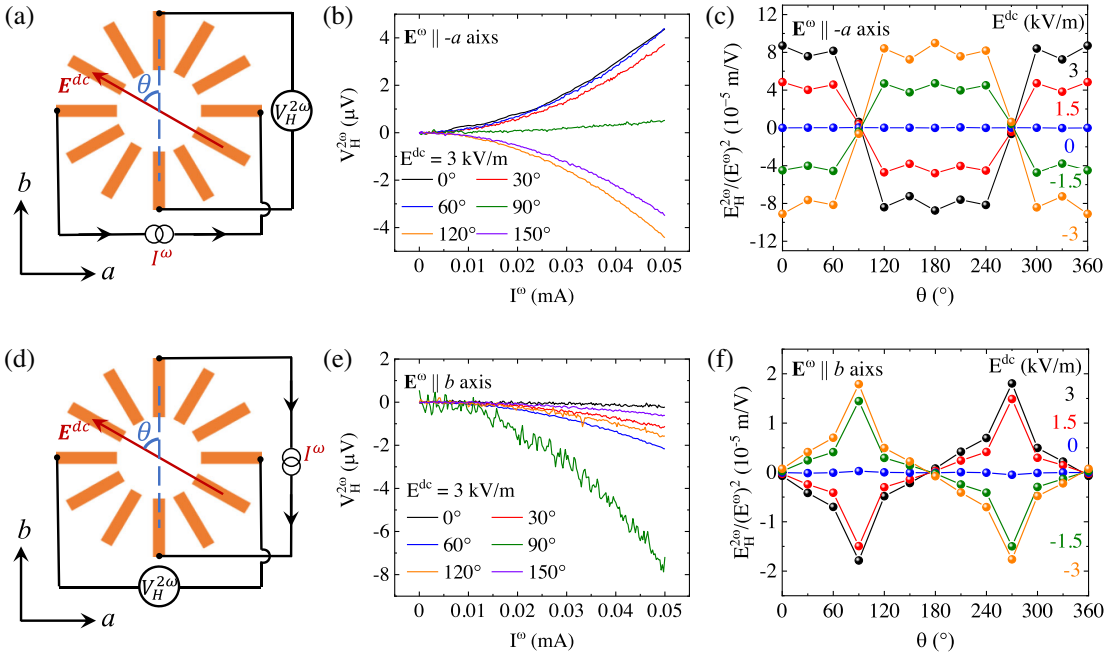

FIG. 2. (a) and (d) Measurement configuration for the second-order AHE with (a) $\mathbf{E}^{\omega}\| -a$ axis and (d) $\mathbf{E}^{\omega}\|b$ axis, respectively. The $\mathbf{E}^{dc}$, satisfying $E^{\mathrm{dc}} \gg E^{\omega}$, is rotated to along various directions. (b) and (e) The second-order Hall voltage $V_H^{2\omega}$ as a function of I^{ω} at fixed $E^{\mathrm{dc}} = 3$ kV/m but along various directions and at 5 K with (b) $\mathbf{E}^{\omega}\| -a$ axis and (e) $\mathbf{E}^{\omega}\|b$ axis, respectively. (c) and (f) The second-order Hall signal $[E_H^{2\omega}/(E^{\omega})^2]$ as a function of θ at 5 K with (c) $\mathbf{E}^{\omega}\| -a$ axis and (f) $\mathbf{E}^{\omega}\|b$ axis, respectively.

voltage $V_H^{2\omega}$ was measured to reveal the nonlinear Hall effect. The $\mathbf{E}^{\mathrm{dc}}$ that is used to produce BCD was applied along the direction characterized by the angle θ, which is the angle between the direction of $\mathbf{E}^{\mathrm{dc}}$ and the baseline of a pair of electrodes [white line in Fig. 1(d)] that is approximately along the b axis. Then $\mathbf{E}^{\mathrm{dc}}$ along $\theta = 0°$ (b axis) and $\theta = 90°$ ($-a$ axis) correspond to the induced $\mathbf{D}^{(1)}$ along the a axis and b axis, respectively. Because the nonlinear Hall voltage $V_H^{2\omega}$ is proportional to $\mathbf{D}^{(1)} \cdot \mathbf{E}^{\omega}$ [9], the nonlinear Hall effect should be observed for $\mathbf{E}^{\omega}\|\mathbf{D}^{(1)}$ and be vanishing for $\mathbf{E}^{\omega}\perp\mathbf{D}^{(1)}$.

As shown in Fig. 1(e), when $\mathbf{E}^{\mathrm{dc}}$ along $\theta = 0°$, nonlinear Hall voltage $V_H^{2\omega}$ is indeed observed as expected. The $\mathbf{E}^{\mathrm{dc}}$ along the b axis induces BCD along the a axis, leading to nonzero $V_H^{2\omega}$ since $\mathbf{E}^{\omega}$ is applied along the $-a$ axis. The second-order nature is verified by both the second-harmonic signal and parabolic I-V characteristics. It is found that the nonlinear Hall voltage is highly tunable by the magnitude of E^{dc}. The sign reverses when E^{dc} is reversed. Moreover, the nonlinear Hall voltage is linearly proportional to E^{dc} (Supplemental Material [29] Fig. S11), as we expected. As for $\mathbf{E}^{\mathrm{dc}}$ along $\theta = 90°$, as shown in Fig. 1(f), the $V_H^{2\omega}$ is much suppressed, which is at least one order of magnitude smaller than the $V_H^{2\omega}$ in Fig. 1(e). Because in this case the $\mathbf{E}^{\mathrm{dc}}$ along the a axis induces BCD along the b axis, $\mathbf{E}^{\omega}$ is almost perpendicular to BCD, leading to negligible nonlinear Hall effect. Similar results are also reproduced in device S2 (Supplemental Material [29], Fig. S12). Such control experiments are well consistent with our theoretical expectation and confirm the validity of field-induced BCD.

Besides the crystalline axis ($\theta = 0°$ and 90°), we also study the case when $\mathbf{E}^{\mathrm{dc}}$ is applied along arbitrary θ directions to obtain the complete angle dependence of field-induced BCD. Here, $\mathbf{E}^{\omega}$ is applied along the $-a$ or b axis, to detect the BCD component along the a or b axis, i.e., $\mathbf{D}^{(1)} = [D_a^{(1)}(\theta), D_b^{(1)}(\theta)]$, where $D_a^{(1)}$ and $D_b^{(1)}$ are the BCD components along the a and b axis, respectively. The measurement configurations are shown in Figs. 2(a) and 2(d). Figures 2(b) and 2(e) show the second-order Hall voltage as a function of θ, with the magnitude of $\mathbf{E}^{\mathrm{dc}}$ fixed at 3 kV/m. The second-order Hall response $[E_H^{2\omega}/(E^{\omega})^2]$ is calculated by $E_H^{2\omega} = (V_H^{2\omega}/W)$ and $E^{\omega} = (I^{\omega}R_{\|}/L)$, where W is the channel width, $R_{\|}$ is the longitudinal resistance, and L is the channel length. As shown in Figs. 2(c) and 2(f), $[E_H^{2\omega}/(E^{\omega})^2]$ demonstrates a strong anisotropy, closely related to the inherent symmetry of WTe_2. First of all, it is worth noting that the second-order Hall signal is negligible at $\mathbf{E}^{\mathrm{dc}} = 0$. This is consistent with our previous analysis that the inherent bulk in-plane BCD is symmetry forbidden [26,27]. Second, $[E_H^{2\omega}/(E^{\omega})^2]$ almost vanishes when $\mathbf{E}^{\mathrm{dc}}\|\mathbf{E}^{\omega}$ along a or b axis. This is constrained by the mirror symmetries M_a or $\tilde{M}_b$, forcing the BCD to be perpendicular to the mirror plane in such configurations.

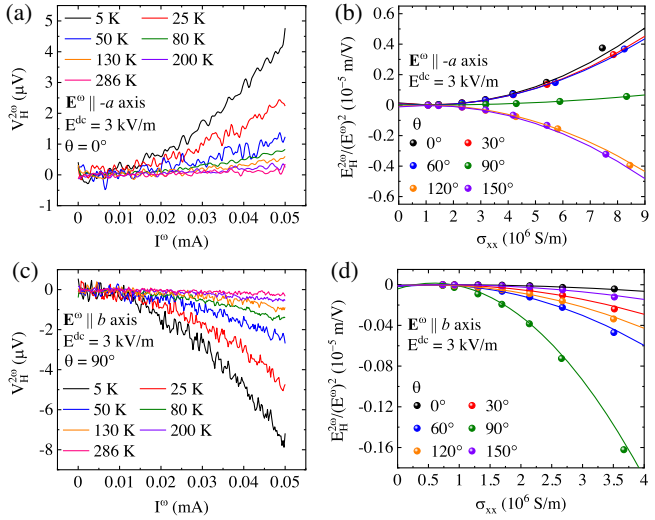

FIG. 3. (a) and (c) The second-harmonic Hall voltage at various temperatures with the magnitude of $\mathbf{E}^{\mathrm{dc}}$ fixed at 3 kV/m (a) under $\mathbf{E}^{\omega}\| -a$ axis, $\theta = 0°$ and (c) under $\mathbf{E}^{\omega}\| b$ axis, $\theta = 90°$. (b),(d) Second-order Hall signal $[E_H^{2\omega}/(E^{\omega})^2]$ as a function of σ_{xx} (b) under $\mathbf{E}^{\omega}\| -a$ axis and (d) under $\mathbf{E}^{\omega}\| b$ axis at various θ with the magnitude of $\mathbf{E}^{\mathrm{dc}}$ fixed at 3 kV/m. The temperature range for the scaling law in (b) and (d) is 50–286 K.

Thus, when $\mathbf{E}^{\mathrm{dc}}\|\mathbf{E}^{\omega}$ along the a or b axis, the induced BCD is perpendicular to $\mathbf{E}^{\mathrm{dc}}$ and $\mathbf{E}^{\omega}$, satisfying $\mathbf{D}^{(1)} \cdot \mathbf{E}^{\omega} = 0$, which leads to almost vanished second-order Hall signals. Moreover, $[E_H^{2\omega}/(E^{\omega})^2]$ exhibits a sensitive dependence on the angle θ, indicating the BCD is highly tunable by the orientation of $\mathbf{E}^{\mathrm{dc}}$. A local minimum of $[E_H^{2\omega}/(E^{\omega})^2]$ is found at an intermediate angle around $\theta = 30°$ when $\mathbf{E}^{\omega}\| -a$ axis in Fig. 2(c). This is because $[E_H^{2\omega}/(E^{\omega})^2]$ depends not only on $(\mathbf{D}^{(1)} \cdot \widehat{\mathbf{E}^{\omega}})$, i.e., the projection of the pseudovector $\mathbf{D}^{(1)}$ to the direction of $\mathbf{E}^{\omega}$, but also on the anisotropy of conductivity in WTe_2. The two terms show different dependence on the angle θ, leading to a local minimum around $\theta = 30°$.

Through control experiments and symmetry analysis, the extrinsic effects, such as diode effect, thermal effect, and thermoelectric effect, could be safely ruled out as the main reason of the observed second-order nonlinear AHE (see Supplemental Material, Note 9 [29]). To further investigate this effect, the temperature dependence and scaling law of the second-order nonlinear Hall signal are studied. By changing the temperature, $V_H^{2\omega}$ and longitudinal conductivity σ_{xx} were collected, where the magnitude of $\mathbf{E}^{\mathrm{dc}}$ was fixed at 3 kV/m. Figures 3(a) and 3(c) show the $V_H^{2\omega}$ at different temperatures with $\mathbf{E}^{\omega}\| -a$ axis, $\theta = 0°$ and $\mathbf{E}^{\omega}\| b$ axis, $\theta = 90°$, respectively. A relatively small but nonzero second-order Hall signal is observed at 286 K. The scaling law, that is, the second-order Hall signal $[E_H^{2\omega}/(E^{\omega})^2]$ versus σ_{xx}, is presented and analyzed in Figs. 3(b) and 3(d) for different angles θ. The σ_{xx} was calculated by $\sigma_{xx} = (1/R_{\|})(L/Wd)$, where d is the thickness of WTe_2, and was varied by changing temperature. According to Ref. [42], the scaling law between $[E_H^{2\omega}/(E^{\omega})^2]$ and σ_{xx} satisfies $[E_H^{2\omega}/(E^{\omega})^2] = C_0 + C_1\sigma_{xx} + C_2\sigma_{xx}^2$. The coefficients C_2 and C_1 involve the mixing contributions from various skew scattering processes [42–45], such as impurity scattering, phonon scattering, and mixed scattering from both phonons and impurities [42]. C_0 is mainly contributed by the intrinsic mechanism, i.e., the field-induced BCD here. As shown in Figs. 3(b) and 3(d), the scaling law is well fitted for all angles θ.

It is found that C_0 shows strong anisotropy (Supplemental Material [29], Fig. S18), indicating the field-induced BCD is also strongly dependent on angle θ. The value of field-induced BCD can be estimated through $D = (2\hbar^2 n/m^* e)[E_H^{2\omega}/(E^{\omega})^2]$ [12], where $\hbar$ is the reduced Planck constant, e is the electron charge, $m^* = 0.3m_e$ is the effective electron mass, n is the carrier density. Here, we replace the $[E_H^{2\omega}/(E^{\omega})^2]$ by the coefficient C_0 from the scaling law fitting. The two components of BCD along the a and b axes, denoted as $D_a^{(1)}$ and $D_b^{(1)}$, are calculated from the fitting curves with the magnitude of $\mathbf{E}^{\mathrm{dc}}$ fixed at 3 kV/m under the $\mathbf{E}^{\omega}\| -a$ axis and the $\mathbf{E}^{\omega}\| b$ axis, respectively. As shown in Figs. 4(a) and 4(b), it is found that $D_a^{(1)}$ shows a $\cos\theta$ dependence on θ, whereas $D_b^{(1)}$

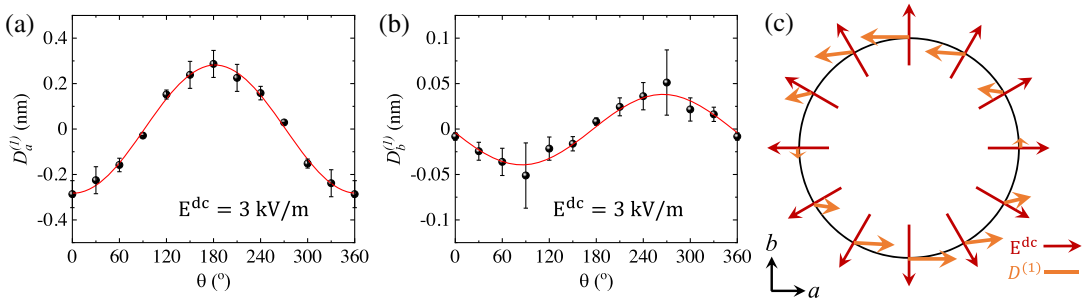

FIG. 4. The induced Berry curvature dipole as a function of θ with the magnitude of $\mathbf{E}^{\mathrm{dc}}$ fixed at 3 kV/m for (a) the component along a axis, $D_a^{(1)}$ and (b) the component along b axis, $D_b^{(1)}$. (c) The relationship between the field-induced Berry curvature dipole $\mathbf{D}^{(1)}$ and the applied $\mathbf{E}^{\mathrm{dc}} = 3$ kV/m along different directions. The scale bar of $D^{(1)}$ is 0.2 nm.

shows a $\sin\theta$ dependence. Such angle dependence is well consistent with the theoretical predications (see Supplemental Material [29], Note 6). According to the two components $D_a^{(1)}$ and $D_b^{(1)}$, the field induced BCD vector of $\mathbf{D}^{(1)}$ is synthesized for $\mathbf{E}^{\mathrm{dc}}$ along various directions, as presented in Fig. 4(c). It is found that both the magnitude and orientation of the field-induced BCD are highly tunable by the dc field.

In summary, we have demonstrated the generation, modulation, and detection of the induced BCD due to the Berry connection polarizability in WTe_2. It is found that the direction of the generated BCD is controlled by the relative orientation between the applied $\mathbf{E}^{\mathrm{dc}}$ direction and the crystal axis, and its magnitude is proportional to the intensity of $\mathbf{E}^{\mathrm{dc}}$. Using independent control of the two applied fields, our Letter demonstrates an efficient approach to probe the nonlinear transport tensor symmetry, which is also helpful for full characterization of nonlinear transport coefficients. Moreover, the manipulation of BCD up to room temperature by electric means without additional symmetry breaking will greatly extend the BCD-related physics [46,47] to more general materials and should be valuable for developing devices utilizing the geometric properties of Bloch electrons.

This work was supported by National Key Research and Development Program of China (No. 2018YFA0703703), National Natural Science Foundation of China (Grants No. 91964201 and No. 61825401), and Singapore MOE AcRF Tier 2 (MOE-T2EP50220-0011). We are grateful to Dr. Yanfeng Ge at SUTD for inspired discussions.

*These authors contributed equally to this work.
†liaozm@pku.edu.cn

[1] N. Nagaosa, J. Sinova, S. Onoda, A. H. MacDonald, and N. P. Ong, Anomalous Hall effect, Rev. Mod. Phys. **82**, 1539 (2010).
[2] J. Sinova, S. O. Valenzuela, J. Wunderlich, C. H. Back, and T. Jungwirth, Spin Hall effects, Rev. Mod. Phys. **87**, 1213 (2015).
[3] D. Xiao, W. Yao, and Q. Niu, Valley-Contrasting Physics in Graphene: Magnetic Moment and Topological Transport, Phys. Rev. Lett. **99**, 236809 (2007).
[4] L. Šmejkal, Y. Mokrousov, B. Yan, and A. H. MacDonald, Topological antiferromagnetic spintronics, Nat. Phys. **14**, 242 (2018).
[5] D. Xiao, M.-C. Chang, and Q. Niu, Berry phase effects on electronic properties, Rev. Mod. Phys. **82**, 1959 (2010).
[6] M.-C. Chang and Q. Niu, Berry phase, hyperorbits, and the Hofstadter spectrum: Semiclassical dynamics in magnetic Bloch bands, Phys. Rev. B **53**, 7010 (1996).
[7] M. T. Dau, C. Vergnaud, A. Marty, C. Beigné, S. Gambarelli, V. Maurel, T. Journot, B. Hyot, T. Guillet, B. Grévin *et al.*, The valley Nernst effect in WSe_2, Nat. Commun. **10**, 5796 (2019).
[8] B.-C. Lin, S. Wang, S. Wiedmann, J.-M. Lu, W.-Z. Zheng, D. Yu, and Z.-M. Liao, Observation of an Odd-Integer Quantum Hall Effect from Topological Surface States in Cd_3As_2, Phys. Rev. Lett. **122**, 036602 (2019).
[9] I. Sodemann and L. Fu, Quantum Nonlinear Hall Effect Induced by Berry Curvature Dipole in Time-Reversal Invariant Materials, Phys. Rev. Lett. **115**, 216806 (2015).
[10] J.-S. You, S. Fang, S.-Y. Xu, E. Kaxiras, and T. Low, Berry curvature dipole current in the transition metal dichalcogenides family, Phys. Rev. B **98**, 121109(R) (2018).
[11] Y. Zhang, J. van den Brink, C. Felser, and B. Yan, Electrically tunable nonlinear anomalous Hall effect in two-dimensional transition-metal dichalcogenides WTe_2 and $MoTe_2$, 2D Mater. **5**, 044001 (2018).
[12] Q. Ma, S.-Y. Xu, H. Shen, D. MacNeill, V. Fatemi, T.-R. Chang, A. M. M. Valdivia, S. Wu, Z. Du, C.-H. Hsu *et al.*, Observation of the nonlinear Hall effect under time-reversal-symmetric conditions, Nature (London) **565**, 337 (2019).
[13] K. Kang, T. Li, E. Sohn, J. Shan, and K. F. Mak, Nonlinear anomalous Hall effect in few-layer WTe_2, Nat. Mater. **18**, 324 (2019).
[14] S.-Y. Xu, Q. Ma, H. Shen, V. Fatemi, S. Wu, T.-R. Chang, G. Chang, A. M. M. Valdivia, C.-K. Chan, Q. D. Gibson, J. Zhou, Z. Liu, K. Watanabe, T. Taniguchi, H. Lin, R. J. Cava, L. Fu, N. Gedik, and P. Jarillo-Herrero, Electrically switchable Berry curvature dipole in the monolayer topological insulator WTe_2, Nat. Phys. **14**, 900 (2018).
[15] J. Xiao, Y. Wang, H. Wang, C. D. Pemmaraju, S. Wang, P. Muscher, E. J. Sie, C. M. Nyby, T. P. Devereaux, X. Qian *et al.*, Berry curvature memory through electrically driven stacking transitions, Nat. Phys. **16**, 1028 (2020).
[16] D. Kumar, C.-H. Hsu, R. Sharma, T.-R. Chang, P. Yu, J. Wang, G. Eda, G. Liang, and H. Yang, Room-temperature nonlinear Hall effect and wireless radiofrequency rectification in Weyl semimetal $TaIrTe_4$, Nat. Nanotechnol. **16**, 421 (2021).
[17] J. Lee, Z. Wang, H. Xie, K. F. Mak, and J. Shan, Valley magnetoelectricity in single-layer MoS_2, Nat. Mater. **16**, 887 (2017).
[18] J. Son, K.-H. Kim, Y. H. Ahn, H.-W. Lee, and J. Lee, Strain Engineering of the Berry Curvature Dipole and Valley Magnetization in Monolayer MoS_2, Phys. Rev. Lett. **123**, 036806 (2019).
[19] M.-S. Qin, P.-F. Zhu, X.-G. Ye, W.-Z. Xu, Z.-H. Song, J. Liang, K. Liu, and Z.-M. Liao, Strain tunable Berry curvature dipole, orbital magnetization and nonlinear Hall effect in WSe_2 monolayer, Chin. Phys. Lett. **38**, 017301 (2021).
[20] M. Huang, Z. Wu, J. Hu, X. Cai, E. Li, L. An, X. Feng, Z. Ye, N. Lin, K. T. Law *et al.*, Giant nonlinear Hall effect in twisted WSe_2, Natl. Sci. Rev. nwac232 (2022).
[21] S.-C. Ho, C.-H. Chang, Y.-C. Hsieh, S.-T. Lo, B. Huang, T.-H.-Y. Vu, C. Ortix, and T.-M. Chen, Hall effects in artificially corrugated bilayer graphene without breaking time-reversal symmetry, Nat. Electron. **4**, 116 (2021).
[22] P. He, H. Isobe, D. Zhu, C.-H. Hsu, L. Fu, and H. Yang, Quantum frequency doubling in the topological insulator Bi_2Se_3, Nat. Commun. **12**, 698 (2021).
[23] O. O. Shvetsov, V. D. Esin, A. V. Timonina, N. N. Kolesnikov, and E. V. Deviatov, Non-linear Hall effect in

three-dimensional Weyl and Dirac semimetals, JETP Lett. **109**, 715 (2019).

[24] S. Dzsaber, X. Yan, M. Taupin, G. Eguchi, A. Prokofiev, T. Shiroka, P. Blaha, O. Rubel, S. E. Grefe, H.-H. Lai *et al.*, Giant spontaneous Hall effect in a nonmagnetic Weyl–Kondo semimetal, Proc. Natl. Acad. Sci. U.S.A. **118**, e2013386118 (2021).

[25] A. Tiwari, F. Chen, S. Zhong, E. Drueke, J. Koo, A. Kaczmarek, C. Xiao, J. Gao, X. Luo, Q. Niu *et al.*, Giant *c*-axis nonlinear anomalous Hall effect in T_d-$MoTe_2$ and WTe_2, Nat. Commun. **12**, 2049 (2021).

[26] S. Lai, H. Liu, Z. Zhang, J. Zhao, X. Feng, N. Wang, C. Tang, Y. Liu, K. S. Novoselov, S. A. Yang *et al.*, Third-order nonlinear Hall effect induced by the Berry-connection polarizability tensor, Nat. Nanotechnol. **16**, 869 (2021).

[27] H. Liu, J. Zhao, Y.-X. Huang, X. Feng, C. Xiao, W. Wu, S. Lai, W.-b. Gao, and S. A. Yang, Berry connection polarizability tensor and third-order Hall effect, Phys. Rev. B **105**, 045118 (2022).

[28] Y. Gao, S. A. Yang, and Q. Niu, Field Induced Positional Shift of Bloch Electrons and Its Dynamical Implications, Phys. Rev. Lett. **112**, 166601 (2014).

[29] See Supplemental Material at http://link.aps.org/supplemental/10.1103/PhysRevLett.130.016301 for device fabrication, electrical measurements, calculation details, polarized Raman spectroscopy of few-layer WTe_2, transport properties of the devices, angle-dependent third-order anomalous Hall effect, symmetry analysis of WTe_2, theory analysis of the field-induced Berry curvature dipole, control experiments in device S2, extrinsic effects that may induce nonlinear transport, and anisotropy of the scaling parameters, which includes Refs. [30–41].

[30] L. Wang, I. Meric, P. Y. Huang, Q. Gao, Y. Gao, H. Tran, T. Taniguchi, K. Watanabe, L. M. Campos, D. A. Muller *et al.*, One-dimensional electrical contact to a two-dimensional material, Science **342**, 614 (2013).

[31] G. Kresse and J. Hafner, Ab initio molecular dynamics for open-shell transition metals, Phys. Rev. B **48**, 13115 (1993).

[32] G. Kresse and J. Furthmüller, Efficient iterative schemes for ab initio total-energy calculations using a plane-wave basis set, Phys. Rev. B **54**, 11169 (1996).

[33] P. E. Blöchl, Projector augmented-wave method, Phys. Rev. B **50**, 17953 (1994).

[34] J. P. Perdew, K. Burke, and M. Ernzerhof, Generalized Gradient Approximation Made Simple, Phys. Rev. Lett. **77**, 3865 (1996).

[35] G. Pizzi *et al.*, Wannier90 as a community code: New features and applications, J. Phys. Condens. Matter **32**, 165902 (2020).

[36] M. Kim, S. Han, J. H. Kim, J.-U. Lee, Z. Lee, and H. Cheong, Determination of the thickness and orientation of few-layer tungsten ditelluride using polarized Raman spectroscopy, 2D Mater. **3**, 034004 (2016).

[37] M. N. Ali, J. Xiong, S. Flynn, J. Tao, Q. D. Gibson, L. M. Schoop, T. Liang, N. Haldolaarachchige, M. Hirschberger, N. P. Ong *et al.*, Large, non-saturating magnetoresistance in WTe_2, Nature (London) **514**, 205 (2014).

[38] V. Fatemi, Q. D. Gibson, K. Watanabe, T. Taniguchi, R. J. Cava, and P. Jarillo-Herrero, Magnetoresistance and quantum oscillations of an electrostatically tuned semimetal-to-metal transition in ultrathin WTe_2, Phys. Rev. B **95**, 041410(R) (2017).

[39] X. Zhang, V. Kakani, J. M. Woods, J. J. Cha, and X. Shi, Thickness dependence of magnetotransport properties of tungsten ditelluride, Phys. Rev. B **104**, 165126 (2021).

[40] T. Akamatsu *et al.*, A van der Waals interface that creates in-plane polarization and a spontaneous photovoltaic effect, Science **372**, 68 (2021).

[41] C. Dames and G. Chen, 1ω, 2ω, and 3ω methods for measurements of thermal properties, Rev. Sci. Instrum. **76**, 124902 (2005).

[42] Z. Z. Du, C. M. Wang, S. Li, H.-Z. Lu, and X. C. Xie, Disorder-induced nonlinear Hall effect with time-reversal symmetry, Nat. Commun. **10**, 3047 (2019).

[43] Y. Tian, L. Ye, and X. Jin, Proper Scaling of the Anomalous Hall Effect, Phys. Rev. Lett. **103**, 087206 (2009).

[44] L. Ye, M. Kang, J. Liu, F. von Cube, C. R. Wicker, T. Suzuki, C. Jozwiak, A. Bostwick, E. Rotenberg, D. C. Bell *et al.*, Massive Dirac fermions in a ferromagnetic kagome metal, Nature (London) **555**, 638 (2018).

[45] H. Isobe, S.-Y. Xu, and L. Fu, High-frequency rectification via chiral Bloch electrons, Sci. Adv. **6**, eaay2497 (2020).

[46] X.-G. Ye, P.-F. Zhu, W.-Z. Xu, N. Shang, K. Liu, and Z.-M. Liao, Orbit-transfer torque driven field-free switching of perpendicular magnetization, Chin. Phys. Lett. **39**, 037303 (2022).

[47] S. Sinha, P. C. Adak, A. Chakraborty, K. Das, K. Debnath, L. D. V. Sangani, K. Watanabe, T. Taniguchi, U. V. Waghmare, A. Agarwal, and M. M. Deshmukh, Berry curvature dipole senses topological transition in a moiré superlattice, Nat. Phys. **18**, 765 (2022).